Sails trim optimisation using CFD and RBF mesh morphing

Sails trim optimisation using CFD and RBF mesh morphing

M.E. Biancolini[1], I.M. Viola[2], M. Riotte[2]

[1] Department of Industrial Engineering, University of Rome "Tor Vergata" (Via Politecnico 1, 00133, Roma, RM, Italy).

Corresponding author. e-mail: biancolini@ing.uniroma2.it tel: +39 06 72597124 fax: +390672592021

[2] Yacht and Superyacht Research Group, School of Marine Science and Technology, Newcastle University, UK

(Armstrong Building, NE1 7RU, UK)

Abstract

The study is focused on the use of mesh morphing to explore different trims of yachts sails. In particular, four trims of the fore and aft sail of a model-scale sailing yacht were modelled leading to 16 configurations in total. Sail pressure distributions were validated with wind-tunnel measurements for all the 16 configurations, and full verification and validation was performed for one of these conditions. The 16 configurations were modelled with two different approaches: generating a new mesh for each trim condition (standard method) and using a morphed version of the baseline condition. This second novel method, based on the use of radial basis functions to morph the mesh, allows the computational time of exploring different geometries with computational fluid dynamics to be significantly decreased. Good agreement is observed between the pressure distributions computed with new meshes and morphed meshes. In order to show an example of trim optimisation, a metamodel approach is defined for the estimation of the response surface using radial basis function interpolation in the parameter space. Thanks to the continuum nature of morphing approach, the optimal trim angles for the given flow condition could be verified using new full computational fluid dynamic simulations. The original full factorial map of 16 points was replaced with a new map of 9 points with an optimal space filling approach to understand the faithfulness of a reduced metamodel. In both cases optimal point is evaluated using a fine Design Of Experiment table built using the metamodel (41 levels for each parameter). The maximum thrust is achieved at the same trim for both metamodels. Proposed method can be easily extended to a wide number of parameters. Such flexibility is demonstrated in the present paper showing the sensitivity of results with respect to apparent wind angle and heeling angle.

Symbols and abbreviations

C_p	Pressure coefficient
CX	Aerodynamic drive force coefficient
CY	Aerodynamic side force coefficient
G	Genoa Sheeting Angle (G1=0°, G2=1.5°, G3=2.9°, G4=4.1°)
h	Generic polynomial
M	Mainsail Sheeting Angle (M1=0°, M2=1°, M3=2°, M4=3°)
n	Dimensions of the design space
N	Number of RBF centres
q	Generic polynomial
r	Distance between two points
Re	Reynolds number
s	Interpolation function composed of an RBF and a polynomial
U_c	Convergence Uncertainty
U_{exp}	Experimental Uncertainty
U_g	Grid Uncertainty
U_{num}	Numerical Uncertainty
U_{val}	Validation Uncertainty
s_x, s_y, s_z	Components of the morphing field
$\boldsymbol{g}$	Vector of the scalar function to be interpolated, evaluated at RBF centres
$\boldsymbol{x}$	Position vector in the Cartesian reference system *O(x,y,z)*
$\widehat{\boldsymbol{x}}$	Vector of RBF centres
$\boldsymbol{M}$	Interpolation matrix used for RBF fit
$\boldsymbol{P}$	Constraint matrix used for RBF fit
φ	Radial Basis Function
$\boldsymbol{\beta}$	Vector of coefficients of the fitted polynomial
$\boldsymbol{\gamma}$	Vector of coefficients of the fitted RBF
AWA	Apparent Wind Angle

CAD	Computer Aided Design
CFD	Computational Fluid Dynamics
DOE	Design of Experiments
FEM	Finite Element Model
RBF	Radial Basis Functions
V&V	Verification and Validation

1. Introduction

1.1 Principles of sail aerodynamics

Yacht sails are designed to maximise the boat speed. In light wind condition, this is achieved by maximising the aerodynamic force component along the boat's heading, while in strong breeze the optimum design depends on the hydrostatic and hydrodynamic characteristics of the boat. For small variation of the sailing conditions, the sail trim is adjusted in order to keep maximising the boat speed.

Sails are thin multi-slotted wings, with relatively small aspect ratio, using very thin airfoil sections and operating at low Reynolds number *(Re)*. In particular, a typical sailing yacht uses two sails in series, the aspect ratio of each sail is between two and three, the sailcloth thickness is smaller than 1% of the chord, and the *Re* is of the order of 10^5 based on the aerodynamic chord. Considering their limited aspect ratio and the low *Re*, modern sails are aerodynamically very efficient. The efficiency of sails is due to complex flow features that are specific to airfoils with sharp leading edges and operating at low *Re*.

The *genoa* is the typical foresail used in light-wind *upwind* conditions, i.e. when the complementary angle between the atmospheric wind velocity at the reference height of $10\ \mathrm{m}$ from the sea level and the boat velocity is smaller than $90°$. The leading edge of the genoa is sharp compared to its chord (the leading edge radius is smaller than 1% of the chord) and this leads to laminar separation at the leading edge on the leeward (suction) side (Figure 1). Transition occurs in the separated shear layer leading to reattachment in the first quarter of the sails, forming the so-called laminar separation bubble associated with a suction peak near the leading edge. Downstream a turbulent boundary layer develops. The sail camber leads to a suction peak around mid chord and thus to a high adverse pressure gradient which leads to trailing edge separation. On the windward (pressure) side, the velocity and pressure gradients are small and a boundary layer develops along the chord (Viola & Flay, 2011).

The *mainsail* is the aft sail and it is used in almost any sailing conditions. Differently from the foresail, the leading edge of the mainsail is attached to the mast, which has an elliptical shape with radii of the order of 10% of the chord (Figure 1). *Re* based on the mast diameter is of the order of 10^4 leading the laminar boundary layer to separate from the mast and reattach on the sail after the laminar-to-turbulent transition. The pressure distributions on the mainsail are similar to those on the genoa, though the mainsail experiences the downwash of the foresails, while the foresail experiences the upwash of the mainsail.

1.2 Numerical modelling of sails

Numerical simulations have been the main design tool for yacht sails since the 1970's, when potential flow codes became very popular (for instance, Milgram 1968a and 1968b). Unfortunately potential flow theory is unable to model the laminar separation bubble and trailing edge separation. The first Reynolds-averaged Navier-Stokes simulation of a genoa and mainsail by Miyata and Lee (Miyata & Lee, 1999) allowed a step change in the numerical simulation accuracy, modelling viscous effects such as separation. However, they over-estimated the drive force coefficient by about 28% and under-estimated the side force coefficient by about 18% compared to wind tunnel data, probably due to the poor grid resolution and to the inability to correctly model trailing edge separation. In recent years, the growth of computational resources enhanced the numerical/experimental agreement achieved by several authors (for instance Yoo and Kim, 2006; Ciortan & Soares, 2007; Masuyama *et al.,* 2007), who validated their simulations with aerodynamic forces.

In 2011, pressures were measured on pressure-tapped rigid sails in a wind tunnel (Viola *et al.,* 2011). These measurements showed the influence of sail trim on the pressure distributions and highlighted the importance of validating numerical simulations with local quantities such as pressures instead of global quantities. In particular, when the sail is trimmed in pulling the foot of the sails closer to the yacht axis and thus increasing the angle of attack, the trailing edge separation line moves upstream leading to a smoother suction peak due to the sail curvature and to a lower base pressure in the separated region. Therefore, the global aerodynamic force rotates towards the back of the boat leading to lower drive force and higher side force.

1.3 Sail design

In the sail industry, it is common practice to use potential flow codes to compute aerodynamic forces for design purposes. The advantage of potential flow codes is the low computational cost, which allows a large number of sail configurations to be explored in a short time. In fact, in order to compare two candidate designs, the optimum performance of each sail must be evaluated across the whole target range of operative conditions. For each condition, the optimum trim must be found. The sail trim depends mainly on the sheeting angle (angle between the boat axis and the sail's foot chord), on the twist angles (angle between the lowest and highest sail's chords) and, with a smaller range of variation, on different cambers and positions of the maximum camber along the chord. In order to find the optimum trim, simulations for all combinations of these parameters should be explored. Also, two different mainsails might show optimum performance for different trims of the headsail, and vice versa. For

instance, a mainsail with a higher camber is likely to prefer a foresail trimmed to a lower sheeting angle allowing a minimum gap between the two sails.

The very large number of parameters to be optimised requires the use of an optimiser and has led to a preference for fast potential flow codes over Navier-Stokes codes. The increased need for accurate estimations of aerodynamic forces and the growth of computational capabilities make Navier-Stokes solvers, more and more attractive. Indeed, Computational Fluid Dynamics (CFD) is already extensively used for the design of high performance sails such as those used in the America's Cup. One of the main drawbacks of the CFD approach is the long time required for the generation of an accurate model. Usually the workflow from CAD geometry to CFD model requires several steps that include: surface meshing, volume meshing, boundary conditions and solver setup. This process makes the exploration of several variations of the original design complex and sometimes unaffordable.

1.4 Mesh morphing

Mesh morphing is emerging as a meaningful approach for the definition of a shape parametric CFD model. New shapes are generated by deforming the mesh of the baseline CFD model, i.e. just updating nodal positions, which requires a negligible computational time compared to any remeshing procedure. Importantly, preserving the same mesh structure eliminates the remeshing noise that can be confused with the effect of the design parameters. Several algorithms have been explored for this task. A common and well-established technique, the Free Form Deformation (FFD; Sederberg, 1986) method, deforms volumes and controls their shape using a trivariate Bernstein polynomial. The method is meshless, so it can be easily implemented in parallel partitioned meshes with hybrid elements. It allows the definition of new interesting shapes but it lacks accurate local surface control. Such accurate control can be achieved using mesh-based methods, for example in the pseudosolid method (Masud, 2007), where an elastic FEM solution is used to propagate the deformation inside. Parallel implementations can in this case be difficult and extra effort is required when surface movements are not known in advance. The meeting point between these two approaches can be achieved using Radial Basis Functions (RBF) interpolation that combines the benefits of a meshless method with great precision. In this case the RBF morphing field is interpolated using a cloud of points with given displacements. Even if there is interesting research demonstrating that RBF can be successfully adopted for the deformation of CFD meshes (Jakobsson, 2007; de Boer, 2007), their numerical cost has limited their application in the past (direct solution grows by N^3 where N is the number of RBF centres). Recent efforts have been devoted to the acceleration of the method to deal with large RBF dataset. Rendall & Allen (2009, 2010)

implemented and then optimised a greedy procedure so that the desired accuracy can be achieved retaining only a small subset of the original RBF cloud, demonstrating their methods for the problem of updating CFD mesh according to high order structural modes predicted using FEA. Estruch *et al.* (2012) proposed a parallel implementation tested to deal with large meshes.

The first industrial implementation of RBF mesh morphing was introduced in 2009 with the software RBF Morph (Biancolini *et al.,* 2009) that comes with a fast RBF solver for the bi-harmonic kernel which performances scales as $N^{1.6}$. A complete description of the tool is given in (Biancolini, 2012) while examples of applications can be found in Caridi & Wade (2012), Cella & Biancolini (2012) and Khondge & Sovani (2012).

1.5 Paper outline

In the present paper, a method for sail trim optimisation using CFD simulations and based on mesh morphing is presented. Firstly, the baseline CFD model is described showing its ability to accurately compute sails' pressure distributions as measured in wind tunnel tests. Then the mesh-morphing algorithm is described introducing the background of RBF. A description of the RBF problem setup for the parameterisation of sail angles is provided; in order to demonstrate the flexibility of the method the parameterisation with respect to the apparent wind angle, AWA (i.e. the complementary angle between the wind experienced by the yacht and the yacht velocity), and heeling angle is provided as well. The optimisation loop based on the response surface approach (RBF interpolation in the parameter space) is then described. Presented results demonstrate the accuracy of morphing versus remeshing by direct comparison of original dataset used in experiments (16 configurations). The sensitivity of results with respect to AWA and heeling angle is then reported. Then Design Of Experiment (DOE) points are used for trim optimisation aiming at maximum drive force using response surface and verifying obtained optimal trims using new CFD simulations. The robustness of the optimisation loop is investigated reducing the number of DOE points. The parametric model is used for a new CFD campaign replacing the original DOE map (16 points full factorial) with a new one (9 points optimal space filling). System responses are compared with respect to local optimum and overall response.

2. Proposed Method

Sails trim optimisation requires a parametric CFD model and a tool able to steer the parameter optimisation. Several steps of this process involve the theory of RBF, for this reason it is presented in a separate section. RBF are in fact the core of the mesh-morphing algorithm and RBF are also used as interpolator in the design variable space.

An accurate CFD model capable of faithfully reproducing experimental results is used as the starting point of the method. By using mesh morphing the fixed baseline model is parametric, i.e. capable of continuously changing its shape according to desired input parameters. In this paper, Mainsail Sheeting Angle and Genoa Sheeting Angle are used as an example. These are the angles between the boat longitudinal axis and the sail's foot chord. AWA and heeling angle are considered as well. To drive the optimisation the parametric model has to be steered. Considering the high cost of each CFD evaluation, a metamodelling approach is used, i.e. a table of design points is first defined. For each point of the table (a pair of angles in this case) a new CFD model is generated and fully computed. Obtained results are then post processed to find the objectives (drive and side force components in this case). A metamodel is used to extrapolate responses (calculated only at DOE points) so that the full response surface is available. Considering that the cost of an evaluation on the response surface is very low, an optimisation algorithm can be easily applied to the metamodel to find optimum points or optimal spaces. Usually selected candidates are recalculated using full CFD calculations to reduce the extrapolation uncertainties. New points are added to the metamodel and a refined response surface is used. Further details are provided in the following sections.

2.1 Experimental model

The CFD simulations presented hereafter model recent wind tunnel experiments where pressures on sail surfaces were measured (Viola *et al,* 2011). In particular, rigid pressure-tapped 1:15th-model-scale genoa and mainsail of an AC33-class yacht were tested at the University of Auckland wind tunnel. The wind tunnel has an open jet test section 7-m wide and 3.5-m high; the wind tunnel floor and roof extend further downstream $5.1\ \mathrm{m}$ and $4.8\ \mathrm{m}$, respectively. Sails were supported by wind-transparent wires $2.7\ \mathrm{m}$ downstream of the jet section. The relative position of the two sails modelled a sailing yacht sailing upright at $AWA = 19°$. Mast and rigging were not modelled, while a horizontal flat plate at the level of the genoa foot was used to model the hull and the water plane. Figure 2 shows the experimental setup. The onset flow was uniform in magnitude and direction (i.e. boundary layer generators and twisted flow devices were not used), and the sails were located outside of the boundary layer of the wind tunnel walls. Surface pressures were measured by means of flush pressure taps. In particular, pressures were measured on both the windward and leeward sides on four horizontal sail sections of the genoa and of the mainsail (Figure 2). Four Genoa Sheeting Angles (G1-4) and four Mainsail Sheeting Angles (M1-4) were tested rotating the sails around the axes defined by the end points of the leading edges (Figure 3) by 1.4° and 1°, respectively. In particular, the Genoa Sheeting Angles were 0, 1.4°, 2.7°, 4.1° for G1, G2, G3 and G4, respectively; while the Mainsail Sheeting

Angles were 0, 1°, 2°, 3° for M1, M2, M3 and M4, respectively. Therefore, 16 trim combinations were tested in total. The baseline sail trim, G3M2, was chosen as the trim allowing the maximum drive force, i.e. the global aerodynamic force component along the boat axis. The Genoa and Mainsail Sheeting Angles are presented with respect to the first trims, G1 and M1 respectively.

2.2 Baseline CFD model

This experiment was modelled with CFD using a hexahedral grid built with ANSYS ICEM CFD (version 12.0.1) and solved with ANSYS Fluent (version 12.0.1). The steady incompressible Reynolds-averaged Navier-Stokes equations for Newtonian fluids were solved with a pressure based solver and a finite volume approach. Turbulence was modelled with $k-\epsilon$ SST turbulence model with low Reynolds correction. The grid allowed $y^+ < 3$ on the leeward side, where regions with separated flow occur, and
$5 < y^+ < 25$ on the windward side, where the boundary layer is attached. The grid of the sails and of the horizontal plane below the sails are shown in Figure 4. A SIMPLEC scheme was used to couple velocity and pressure. Second order accuracy discretization algorithms were used because third order accuracy algorithms showed difficulty converging. Simulations were performed with an Intel Core i5 processor 3.2 GHz, 3 GB of RAM and Windows XP Professional operating system.

2.3 Background of Radial Basis Functions

As introduced in section 1.4, RBF are used to produce a solution for mesh movement/morphing, from a list of source points and their displacements (see Schaback, 2007 to learn more about RBF usage). This approach is valid for both surface shape changes and volume mesh smoothing. The same method can be used in generic *n*-dimensional spaces and so provides an effective interpolation tool for the evaluation of the Response Surface.

RBF are a very powerful tool created for the interpolation of scattered data; they are able to interpolate everywhere within the space of a function that is defined at discrete points giving the exact value at original points. The behaviour of the function between the points depends on the kind of RBF adopted. RBF can be fully or compactly supported, some functions require a polynomial correction.

Typical RBF with global and compact support are identified in Table 1. It should be noted that RBF are scalar functions with a scalar variable *r*, which is the Euclidean distance between two points defined in a generic *n*-dimensional space (*n = 2,3* for mesh morphing applications).

As will be shown in detail, a linear system of equations needs to be solved for the coefficients calculation. Once the unknown coefficients are calculated, the motion of an arbitrary point inside or outside the domain (interpolation/extrapolation) is expressed as the sum of the radial contribution of each source point (if the point falls inside the influence domain).

Details of this theory are given using some equations. An interpolation function composed of a radial basis function φ and a polynomial h is defined as follows:

$$s(\boldsymbol{x}) = \sum_{i=1}^{N} \gamma_i \varphi(\|\boldsymbol{x} - \hat{\boldsymbol{x}}_i\|) + h(\boldsymbol{x}) \tag{1}$$

Where $\hat{x}$ is the position of the N RBF centres.

The degree of the polynomial has to be chosen depending on the kind of RBF adopted. A radial basis fit exists if the coefficients γ_i and the weights of the polynomial can be found such that the desired function values $\boldsymbol{g}_i$ are obtained at source points $\hat{\boldsymbol{x}}_i$,

$$s(\hat{\boldsymbol{x}}_{\boldsymbol{i}}) = \boldsymbol{g}_i, 1 \leq i \leq N \tag{2}$$

and the polynomial term gives no contributions at source points.

$$\sum_{i=1}^{N} \gamma_i q(\hat{\boldsymbol{x}}_{\boldsymbol{i}}) = 0 \tag{3}$$

for all polynomials q with a degree less or equal to that of polynomial h. The minimal degree of polynomial h depends on the choice of the RBF. A unique interpolant exists if the basis function is a conditionally positive definite function. If the RBF are conditionally positive definite of order $m \leq 2$, a linear polynomial can be used:

$$h(\boldsymbol{x}) = \beta_1 + \beta_2 x + \beta_3 y + \beta_4 z \tag{4}$$

The subsequent exposition will assume that the aforementioned hypothesis is valid. A consequence of using a linear polynomial is that rigid body translations are exactly recovered. The values for the coefficients γ_i of RBF and the coefficients β of the linear polynomial can be obtained by solving the linear system (order N+4):

$$\begin{pmatrix} \boldsymbol{M} & \boldsymbol{P} \\ \boldsymbol{P^T} & \boldsymbol{0} \end{pmatrix} \begin{pmatrix} \boldsymbol{\gamma} \\ \boldsymbol{\beta} \end{pmatrix} = \begin{pmatrix} \boldsymbol{g} \\ \boldsymbol{0} \end{pmatrix} \tag{5}$$

Where $\boldsymbol{M}$ is the interpolation matrix defined by calculating all the radial interactions between source points:

$$M_{ij} = \varphi\left(\left\|\hat{\boldsymbol{x}}_{\boldsymbol{i}} - \hat{\boldsymbol{x}}_{\boldsymbol{j}}\right\|\right), 1 \leq i \leq N, 1 \leq j \leq N \tag{6}$$

and $\boldsymbol{P}$ (eq. 7) is a constraint matrix that arises to balance the polynomial contribution and contains a column of ones and the *x y z* positions of source points in the others three columns; the control points selected should not be contained in the same plane otherwise the interpolation matrix would be singular.

$$\boldsymbol{P} = \begin{pmatrix} 1 & \hat{\boldsymbol{x}}_{\boldsymbol{1}} & \hat{\boldsymbol{y}}_{\boldsymbol{1}} & \hat{\boldsymbol{z}}_{\boldsymbol{1}} \\ 1 & \hat{\boldsymbol{x}}_{\boldsymbol{2}} & \hat{\boldsymbol{y}}_{\boldsymbol{2}} & \hat{\boldsymbol{z}}_{\boldsymbol{2}} \\ \vdots & \vdots & \vdots & \vdots \\ 1 & \hat{\boldsymbol{x}}_{\boldsymbol{N}} & \hat{\boldsymbol{y}}_{\boldsymbol{N}} & \hat{\boldsymbol{z}}_{\boldsymbol{N}} \end{pmatrix} \tag{7}$$

For the smoothing problem each component of the displacement field prescribed at the source points is interpolated as follows:

$$\begin{cases} s_x(\boldsymbol{x}) = \sum_{i=1}^{N} \gamma_i^x \varphi(\|\boldsymbol{x} - \hat{\boldsymbol{x}}_{\boldsymbol{i}}\|) + \beta_1^x + \beta_2^x x + \beta_3^x y + \beta_4^x z \\ s_y(\boldsymbol{x}) = \sum_{i=1}^{N} \gamma_i^y \varphi(\|\boldsymbol{x} - \hat{\boldsymbol{x}}_{\boldsymbol{i}}\|) + \beta_1^y + \beta_2^y x + \beta_3^y y + \beta_4^y z \\ s_z(\boldsymbol{x}) = \sum_{i=1}^{N} \gamma_i^z \varphi(\|\boldsymbol{x} - \hat{\boldsymbol{x}}_{\boldsymbol{i}}\|) + \beta_1^z + \beta_2^z x + \beta_3^z y + \beta_4^z z \end{cases} \tag{8}$$

The radial basis method has several advantages that make it very attractive for mesh smoothing. The key point is that being a meshless method only grid points are moved regardless of which elements are connected and it is suitable for parallel implementation. In fact, once the solution is known and shared in the memory of each calculation node of the cluster, each partition has the ability to smooth its nodes without taking care of what happens outside because the smoother is a global point function and the continuity at interfaces is implicitly guaranteed. Furthermore, despite its meshless nature, the method is able to exactly prescribe known deformations onto the surface mesh; this effect is achieved by using all the mesh nodes as RBF centres with prescribed displacements, including the simple zero field to guarantee that a surface is left untouched by the morphing action.
It is interesting to note that RBF can be used to fit scalar functions defined in generic n-dimensional spaces and have proven to be an excellent tool for the evaluation of metamodels and Response Surface (Jin *et al.,* 2001).
In this paper we have used direct method for DOE post processing (Lapack solver included in Mathcad software), with the RBF spline $\varphi(r) = r^3$. For mesh morphing the fast solver of RBF Morph was chosen using bi-harmonic kernel $\varphi(r) = r$. Many successful fast RBF approaches are found in literature; among them we recall the Partition Of Unity method (Wendland, 2002) and the Fast Multipole Method (Beatson, 2007).

2.4 RBF setup for sail angles

The RBF Morph software has been used to define two sail trim parameters: the Mainsail Sheeting Angle and the Foresail Sheeting Angle. The setup for the two shape modifiers is similar, so they will be described together.

Two surface sets that contain the nodes of each sail are defined. Nodes extracted from the surface highlighted in Figure 4 are used as RBF centres to carefully control sail shapes assigning a rigid rotation about one sail axis whilst keeping fixed the points on the other one; reference rotation is 1° so the amplification applied to the shape modification will express the sail rotation in degrees. It is important to note that the software comes with a non-linear amplification algorithm that allows proper amplifying rotation without the need to regenerate the RBF fit.

The morphing action of the sail surface has to be limited. Three strategies are described in literature: Rendall & Allen (2009, 2010) use compact support RBF (Wendland C2), so the morphing effect vanishes at support radius distance from the surface; Keye (2009) shows that better mesh quality can be achieved using global support RBF, in this case a zero displacement is imposed at the CFD nodes of the farfield used as fixed RBF centres; Cella & Biancolini (2012) demonstrated that the same mesh quality can be achieved at a substantial reduced cost limiting the morphing action with an Encapsulation volume. The latter approach is used in the present study (Figure 5); RBF centres with a null displacement are added on a cylindrical surface with a spacing defined by the user; such spacing has to be tuned to enforce a vanishing RBF field at Encapsulation border (an optimal value 0.15 m has been used for this study). Encapsulation geometry will be used during the morphing stage to exclude the external part of the mesh from the RBF processing.

The overall RBF problem is composed in this case by 4,156 centres and takes about 4 seconds for fitting (Figure 6).

Obtained shape modifiers are verified using preview tools. A combination of both shape modifier at the maximum values (i.e. 4.1° for Genoa Sheeting Angle and 3.0° for Mainsail Sheeting Angle) are used to observe the surface mesh; the original mesh is also represented to clearly highlight the extent of the shape modification (Figure 7).

As shown the preview is conducted in the horizontal plane at 1-m height with respect to the base plate, the deformation is propagated in the volume mesh, accurately preserving the shape of the volume mesh (Figure 8).

The effect of shape modifiers at the maximum height (acting separately, see Figure 9), is highlighted on a wireframe representation of the aforementioned mesh cut. Original and deformed meshes are in this case superimposed using an orthographic view from the top.

A complete morphing action, using a combination of both shape modifiers, takes approximately 90 seconds in serial and approximately 30 seconds running on 4 cores. The mesh is relatively small (1.5 million nodes), however the

method scales very well in parallel and can be used with meshes of hundreds of millions of cells in a reasonable time. As an example Cella & Biancolini (2012) stressed the RBF solver using a setup of about 430.000 points to morph a 14 millions hexahedrons mesh (i.e. about 14 millions of nodes). It takes 1337 s to fit and 5445 s to morph on a quadcore.

Table 2 shows that, in the relevant range, the quality of the mesh is very well preserved (the maximum reduction of Minimum Orthogonal Quality is about 13%).

2.5 RBF setup for AWA and heeling angles

As exposed in the previous section, the mesh morphing tools is expressive enough so that several shape modifications can be introduced. The actual limit of the method is posed by the quality of the morphed mesh. Among possible shape modifications relevant for this application we have already considered in the past the effect of twist, camber and draft of each sail (Proietti 2012), Figure 10. In that case each sail was controlled using four parameters; the RBF setup was refined so that five cross section of each sail were controlled distributing desired parameter change along the sail length.

In this section the mesh morphing setup used to introduce AWA and heeling angles is addressed. The AWA angle is controlled using the two cylindrical Encaps represented in Figure 11. A 0.2-m spacing is used to distribute 3300 RBF points on the cylinders. This technique is straightforward and effective for any boat configuration. The mesh contained in the internal cylinder undergo a rigid movement (in this case a rotation about the cylinder axis); such movement is propagated outside thanks to RBF points, and it is limited at the external cylinder where RBF points are fixed, so that only the mesh included in the space enclosed between the two Encaps is deformed (Figure 12).

The heeling angle is more difficult to control, especially for this experimental configuration in which the Genoa intersects the plate. A first setup was defined imposing desired heeling rotation at both sails, leaving the portion of the Genoa between the plate and the mainsail base height free to deform; and imposing a fixed constraint to all the points on the plate; a Domain Encap was then used to complete this. However the shape achieved at the deformable part of the Genoa, resulting from the overall setup, was not good enough. So the setup was improved using two steps approach. In the first step the morphing of Genoa surface is addressed imposing a rigid rotation to the points of the upper part of the sail (leaving a deformable buffer); the points at the intersection between the sail and the plate are constrained (Figure 13). Resulting deformed shape of the sail in this case is very good. The second step setup, used for volume morphing, is identical to the one used for Sheeting Angles, but the movement imposed to the

sails is different. The Main Sail is rotated about the heeling axis, the Genoa is rotated using the first step result that guarantees desired shape at the overall Sail, including the deformable part (Figure 14).

With said approaches, AWA from $17°$ to $29°$ deg and heeling angles from $-1°$ to $20°$ were tested.

2.6 Response surface optimisation

A response surface method known also as surrogate model method or metamodel method, is a well-established technique for the optimisation of costly functions. A DOE table (Design of Experiment) is first populated by sampling values in the design space. Each design parameter can be combined with the others at various levels. In this paper the response surface method is used to optimise the combined effect of two parameters, Mainsail Sheeting Angle and Genoa Sheeting Angle. Two strategies are considered and compared to explore the design space: the full factorial approach and the optimal space filling approach. The former is the one used for experiments in which all the combinations of input parameter at 4 levels are considered, producing 16 entries in the DOE table. System response can be better recovered using a different approach with a lower number of points and an optimal space filling approach that avoids having samples in which a parameter is at the same levels. The DOE table is generated in this case using the optimisation software DX (Design eXplorer) by ANSYS.

3. Results

3.1 Validation of the CFD baseline model

The CFD simulations performed with a standard remeshing approach were validated with wind tunnel data. Good agreement was found between the numerical and experimental pressure distributions for all the 16 configurations. For instance, Figure 15 shows the pressure coefficient C_p measured and computed for the baseline trim G3M2. The largest numerical-experimental differences are observed near the leading edge on both the windward and leeward side. It is believed that the differences on the windward side are due to the use of zero-thickness surfaces to model the sails which, indeed, in the experimental test had a thickness of about 1% of the sail chord and were chamfered at about 20° to produce a sharp leading edge. The difference on the leeward side at the top sections of the genoa and the mainsail is believed to be due to an inaccuracy in the geometry definition, leading to small differences in the local angle of attack. In fact, near the ideal angle of attack, a small change in the angle of attack leads to a large change in the leading edge suction peak. Similar agreement and differences were also found for the other trims.

Verification and validation (V&V) were performed for the baseline trim G3M2 assessing the uncertainty due to the grid *(U_g)*, convergence *(U_c)* and round off *(U_r),* for the L_2 norm of C_p on the four sail sections following the guidelines in Eça *et al.* (2010). U_r was found to be negligible and thus the numerical uncertainty *(U_{num})* was found computing the L_2 norm of U_g and U_c. For every sail section, the differences between the numerical and experimental L_2 norms of C_p were lower than the validation uncertainty *(U_{val})*, which was computed with the L_2 norm of the numerical and experimental *(U_{exp})* uncertainties. Table 3 summarises the V&V results.

3. 2 Comparison between morphing and remeshing

The proposed mesh morphing approach has been validated considering as a reference the re-meshing method results. The morphing technique was used to compute the pressure distribution C_p on each section of each genoa from G1 to G4 with the mainsail fixed. The same task was done on the mainsail with the genoa fixed. Instead of computing the pressure on sails at the four wind-tunnel positions only (G1-4), the morphing technique was also used to explore intermediate trims using its parametric aspect. The corresponding intermediate sail positions are numbered as G12, G23 and G34 for the genoa so that, for instance, G12 correspond to the equidistant position from G1 and G2 (see Figure 16).

The same designation is used for mainsail's intermediate positions (M12, M23 and M34). All the results were collected in one simulation (run) including all the trims, as described in Figure 17: the sails were set to the trim G1M4, the CFD solver was run until convergence was achieved, C_p on the genoa were saved, then the mesh was morphed to trim G2M4, and so forth. Obtained data is represented in Figure 18 where the aerodynamic drive (CX) and side (CY) force coefficients, obtained for the aforementioned morphing analysis, are plotted against relevant angles. Values obtained by full remeshing (when available) are included in the same plot showing an excellent agreement. A quantitative estimation of differences between re-meshing and morphing are summarized in Table 4 as percentage difference (using re-meshing as baseline). Differences are very small, with a maximum of about 0.3%. It is important to note that, in this case, ICEM re-meshing is very close to morphing because all the meshes are generated to the same rules, i.e. preserving the number of cells and topology, and low scatter is found. Conversely, in typical industrial applications, a larger scatter in the re-meshing results is quite common for unstructured meshes. One of the main advantages of mesh morphing with respect to remeshing is that such re-meshing noise is avoided because mesh topology is preserved even for non-structured meshes.

To carefully compare the re-meshing and morphing approaches, pressure coefficient evolution is presented along section 3 of the mainsail in Figure 19 with a fixed genoa. The results show an excellent agreement, shown in Figure 20. The most significant differences are near the leading edge on the leeward side. As it was shown in previous investigations, the C_p prediction is highly sensitive to the angle of attack and therefore, in our case, a small difference between the sail positions after rotation by morphing and the fixed sail positions of the numerical shapes used in re-meshing can lead to different values. However, this plot shows that for these positions, the morphing solution is reliable and can be used instead of re-meshing.

Figure 21 shows the computed C_p for intermediate positions of the mainsail along section 3. A continuous evolution is evident as local C_p values for each intermediate position are equidistant from those computed at wind-tunnel positions. This is particularly visible near the leading edge. The more the sail is eased, the more the leading-edge suction peak is damped, and the higher the pressure is on the leeward side of the section. Conversely, the pressure decreases at the leading edge of the windward side when the sail is eased.

This plot shows that in the observed range, the morphing solution is reliable and could be used to find the optimum trim. As will be shown in the next sections, the optimisation can be easily automated using the ANSYS tool DesignXplorer. Creating all the grids using re-meshing method took approximately 4 days including overnight simulations. These four days include preparation of the new grid with the new trim, preparation of the simulation and simulation itself. On the other hand, the morphing took 15 hours to compute all the 14 trims and requires about one day to prepare the journal file and perform some preliminary testing.

3.3 Sensitivity to AWA and heeling angles

The effect of AWA and heeling angle on CX and CY is represented in Figure 22. In particular, the angle variation from the reference AWA ($\mathrm{AWA} - 19°$) is used. The base line used for this investigation is the trim G1M1, i.e. where both the genoa and the mainsail are maximum tighten. The trim allowing the maximum CX at $\mathrm{AWA} = 19°$ and $\mathrm{heel} = 0°$ is G3M2, which is a tighter trim than the one allowing the maximum lift over drag ratio, and a looser trim than the one allowing the maximum lift. The trim G1M1 allows lower CX than G3M2 but higher lift. Increasing the AWA from $17°$ to $25°$, the lift increases. At such low AWAs, CY shows a similar trend to the lift, while CX increases because the angle between the boat heading and the resultant aerodynamic force decreases. Conversely, for $25° < \mathrm{AWA} < 29°$, the lift and CY reach a plateau while CX decreases because the drag increases.

CX and CY are maximum when the boat is upright ($\mathrm{heel} = 0°$). Increasing the heel angle, CX and CY decrease gently.

In fact, the wind speed in the plane perpendicular to the mast decreases with the cosine of the heel angle and, thus, the aerodynamic forces decrease with approximately the square of the cosine of the heel angle.

3.4 Automated Optimisation Process

Two different tables have been considered (Table 5 and Table 6). A 16 points full factorial one (i.e. the same used for experiments and remeshing) and a 9 points table generated using the optimal space filling algorithm of DX. Columns 2 and 3 contain the input angles. The automated run allows the table (columns 3 and 4) to be completed with the output data, i.e. CX and CY values of each trim configuration. To clearly understand how the design space is filled, the points of both distributions are represented together in Figure 23 as a G-M plot together with corresponding output parameters (i.e. CX and Cy pairs) in the CX-CY plane.

A RBF metamodel has been defined for both tables using $\varphi(r) = r^3$as radial function. A fine table is then defined (1681 points, 41 levels for each parameter). The response in the CX CY plane is represented in Figure 24 for both DOE tables. It is important to highlight that the interesting design locus (Pareto curve) is the upper boundary of the shape representing the maximum CX at various CY levels. It seems that a better resolution is achieved with the 16-point distribution whilst the CX peak is similar for both tables.

It's interesting to note that at the used resolution (i.e. 41 levels) the peak is predicted at the same G-M pair (i.e. $G_{opt}M_{opt}$ 3.28° 1.125°) as the points retrieved from the experiments (and in full factorial 16 points table) at G3M2 (i.e. 2.9° 1.0°). So the $G_{opt}M_{opt}$ point has been fully recomputed using CFD to understand how faithful it is to the metamodel estimation. Figure 24 represents both optimum points (a filled circle represents the peak computed using current metamodel whilst the filled triangle represent the value computed using CFD at $G_{opt}M_{opt}$). Despite the reduced number of points of optimal space filling distribution, the peak estimated using such a distribution is almost identical to the value predicted using a full calculation. The differences are: dCX=0.205% and dCY=0.014% for the 9 points distribution and dCX=0.9% and dCY=0.035% for the 16 points distribution.

4. Conclusions

A method for trim optimisation has been presented. The theory of Radial Basis Functions is used as the base of a mesh morphing approach that allows the use of mesh parameterisation as an interpolator for the evaluation of the Response Surface in the optimisation loop.

The quality of the morphed meshes for this specific application has been demonstrated comparing the results obtained with new high quality meshes and morphed ones. The maximum difference in the aerodynamic drive and

side forces is about 0.3%. The excellent agreement between CFD prediction from re-meshing and from morphing is confirmed by direct comparison of sail surface pressure distributions.

The flexibility of the method is then demonstrated reviewing other relevant shape modifications, as twist, camber and draft of each sail, and AWA and heeling angles. The latter has been fully demonstrated considering both morphing setup and sensitivity analysis, considering that are part of on-going research.

The effectiveness of the new parametric model using mesh morphing has been investigated implementing an optimisation loop. The run has been fully automated using ANSYS Workbench and a custom post processing using MathCAD showing how the optimum point calculated on the Response Surface corresponds to an optimum result after a full CFD calculation (with a max difference of about 0.2% using optimal space filling and lower than 1% using full factorial).

The approach could be easily extended increasing the complexity of shape modifications, accounting for twist camber and draft; and/or increasing the complexity of the system, here a simple configuration has been addressed because of the availability of experimental results.

Response surface method and optimal space filling could be used to drive future experiments and as a tool to quickly represent the response of the sails in the simulation of an actual mission or as an on-line tool for real-time sail control.

As a concluding remark we believe that the morphing approach is so fast that a real virtual wind-tunnel with a real-time Velocity Prediction Program (VPP) can be implemented and can allow, for instance, new investigations with different sail shapes to be performed in the future, including (but not limiting) the ones already cited in the present study.

5. Acknowledgment

The support of Samerio Ramirez to show the sensitivity of results with respect to apparent wind angle and heeling angle is gratefully acknowledged.

6. References

Caridi, D. & Wade, A. (2012). Higher-Speed CFD. *Professional Motorsport Magazine*. April-June 2012, p 56. www.pmw-magazine.com

Beatson, R.K. , Powell, M.J.D. & Tan, A.M. (2007). Fast evaluation of polyharmonic splines in three dimensions. , IMA Journal of Numerical Analysis (2007) 27, 427–450.

Biancolini, M.E., Biancolini, C., Costa, E., Gattamelata, D. & Valentini, P.P. (2009). Industrial Application of the Meshless Morpher RBF Morph to a Motorbike Windshield Optimisation. *In the proceedings of The European Automotive Simulation Conference (EASC)*, 6-7 July 2009, Munich, Germany.

Biancolini, M. E. (2012). Mesh Morphing and Smoothing by Means of Radial Basis Functions (RBF): A Practical Example Using Fluent and RBF Morph. *Handbook of Research on Computational Science and Engineering: Theory and Practice*, IGI Global, ISBN13: 9781613501160.

Cella, U., Biancolini, M. (2012). Aeroelastic Analysis of Aircraft Wind-Tunnel Model Coupling Structural and Fluid Dynamic Codes. *Journal of Aircraft*, 49(2), 407-414.

Ciortan, C., Soares, C.G. (2007). Computational Study of Sail Performance in Upwind Condition. *Ocean Engineering,* 34, 2198–2206.

de Boer, A., van der Schoot, M.S., Bijl, H. (2007). Mesh Deformation Based on Radial Basis Function Interpolation. *Computers and Structures*, June - July, 85 (11-14), 784-795.

Eça, L., Vaz, G., Hoekstra, M. (2010). Code Verification, Solution Verification and Validation in RANS Solvers. *In the proceedings of The ASME 29th International Conference OMAE2010*, 6-11 June, Shanghai, China.

Estruch, O., Lehmkuhl, O., Borrell, R., Pérez Segarra, C.D., Oliva, A. (2012). A Parallel Radial Basis Function Interpolation Method for Unstructured Dynamic Meshes, *Computers & Fluids*, June, 80:44-54,

2013.

Khondge, A., Sovani, S. (2012). An Accurate, Extensive, and Rapid Method for Aerodynamics Optimization: The 50:50:50 Method. *SAE Technical Paper*, 2012-01-0174, doi:10.4271/2012-01-0174.

Masud, A., Bhanabhagvanwala, M., Khurram, R. A. (2007). An Adaptive Mesh Rezoning Scheme for Moving Boundary Flows and Fluid–Structure Interaction. *Computers and Fluids*, January, 36 (1), 77-91.

Masuyama, Y., Tahara, Y., Fukasawa, T., Maeda, N. (2007). Database of Sail Shapes vs. Sail Performance and Validation of Numerical Calculation for Upwind Condition. *In the proceedings of The 18th Chesapeake Sailing Yacht Symposium*, March 2-3, Annapolis, Maryland, USA.

Milgram, J.H. (1968a). The Aeodynamics of Sails. *In the proceedings of The 7th Symposium of Naval Hydrodynamics*, 1397–1434.

Milgram,J.H. (1968b). The Analytical Design of Yacht Sails. *In the proceedings of The SNAME Annual Meeting*, 118–160.

Miyata, H., Lee, Y.W. (1999). Application of CFD Simulation to the Design of Sails, *Journal of Marine Science and Technology*, 4, 163–172.

Proietti, D., final dissertation of Bachelor Thesis "Sail Trim Optimisation" University of Rome Tor Vergata, Rome, 2012.

Rendall, T.C.S., Allen, C.B. (2009). Efficient Mesh Motion using Radial Basis Functions with Data Reduction Algorithms, *Journal of Computational Physics,* 228, 6231–6249

Rendall, T.C.S., Allen, C.B. (2010). Reduced Surface Point Selection Options for Efficient Mesh Deformation Using Radial Basis Functions, *Journal of Computational Physics,* 229, 2810–2820

Sederberg, T, W., Parry, S., R. (1986). Free-Form Deformation of Solid Geometric Models. *In the proceedings of the 13th Annual Conference on Computer Graphics and Interactive Techniques (SIGGRAPH '86)*, David C. Evans and Russell J. Athay (Eds.). ACM, New York, NY, USA, 151-160.

Schaback, R. (2007). A Practical Guide to Radial Basis Functions, April 16, 2007. Retrieved 28/2/2011 from http://num.math.uni-goettingen.de/schaback/teaching/texte/approx/sc.pdf.

Jakobsson, S., Amoignon, O. (2007). Mesh Deformation using Radial Basis Functions for Gradient Based Aerodynamic Shape Optimization, *Computers and Fluids*, July, 36 (6), 1119-1136.

Keye, S. (2009). Fluid-Structure Coupled Analysis of a Transport Aircraft and Comparison to Flight Data. *In the proceedings of The 39th AIAA Fluid Dynamics Conference*, AIAA-2009-4198.

Jin, R., Chen,W., Simpson, T.W. (2001). Comparative Studies of Metamodelling Techniques under multiple Modelling Criteria. *Structural and Multidisciplinary Optimization*, 23, 1–13.

Viola, I.M., Flay R.G.J. (2011). Sail Aerodynamics: Understanding Pressure Distributions on Upwind Sails, *Experimental Thermal and Fluid Science,* 35 (8), 1497-1504.

Viola I.M., Pilate J., Flay R.G.J. (2011). Upwind Sail Aerodynamics: a Pressure Distribution Database for the Validation of Numerical Codes, *International Journal of Small Craft Technology, Trans. RINA,* 153 (B1), 47-58.

Wendland, H. (2002). Fast evaluation of radial basis functions: methods based on partition of unity. In: Chui, C.K., Schumaker, L.L. & Stöckler, J. (2002) Editors, Approximation theory X: wavelets, splines, and applications, Vanderbilt University Press, pp. 473–483.

Yoo, J., Kim, H.T. (2006). Computational and Experimental Study on Performance of Sail of a Sailing Yacht. *Ocean Engineering*, 33, 1322–1342.

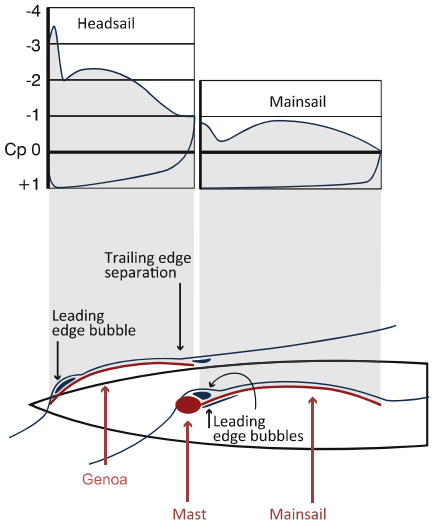

Figure 1: Schematic diagram of the flow and pressure fields around sails in upwind conditions.

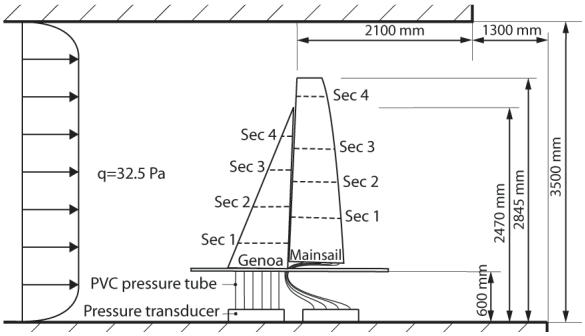

Figure 2: Experimental setup in the wind tunnel.

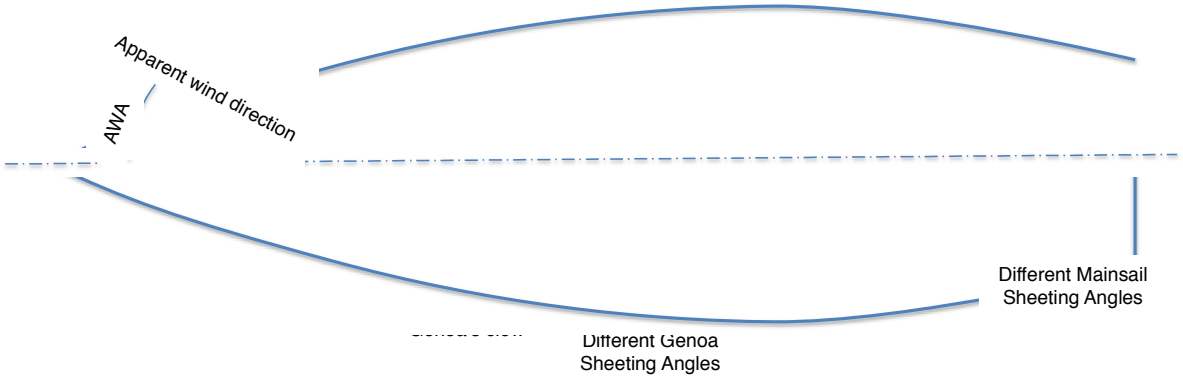

Figure 3: Designation of the wind-tunnel sail positions.

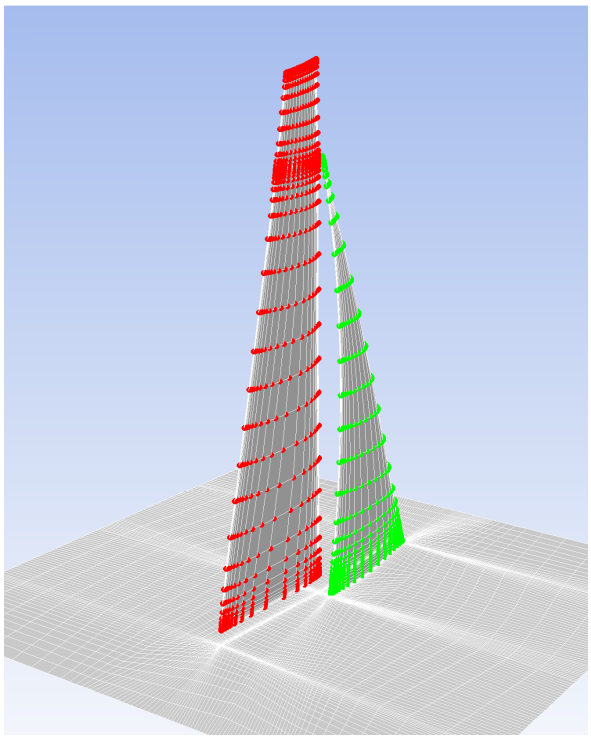

Figure 4: Baseline grid. The highlighted dots show the thread points of the genoa and mainsail.

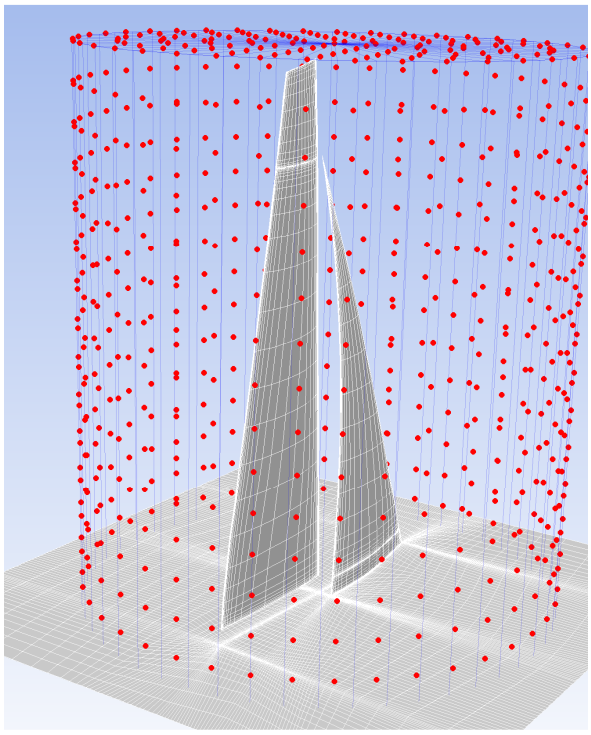

Figure 5: Encapsulation cylinder used to limit the morphing action.

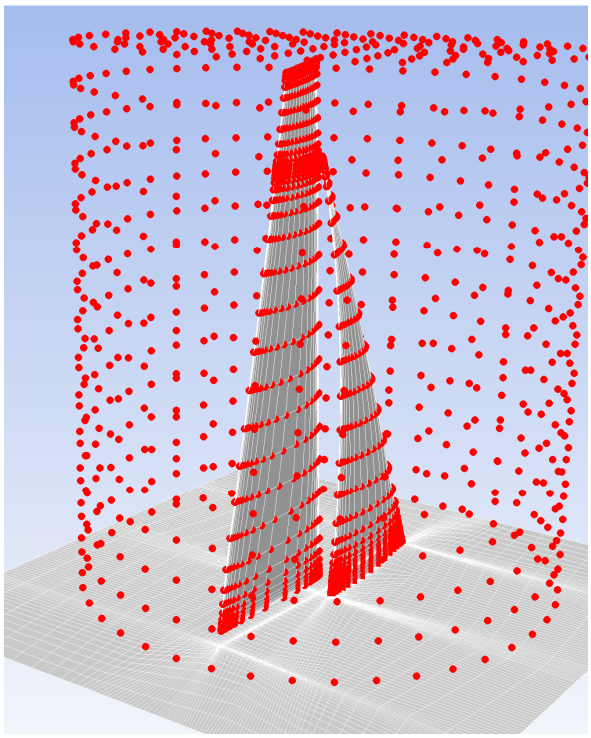

Figure 6: Full RBF problem, all source points shown.

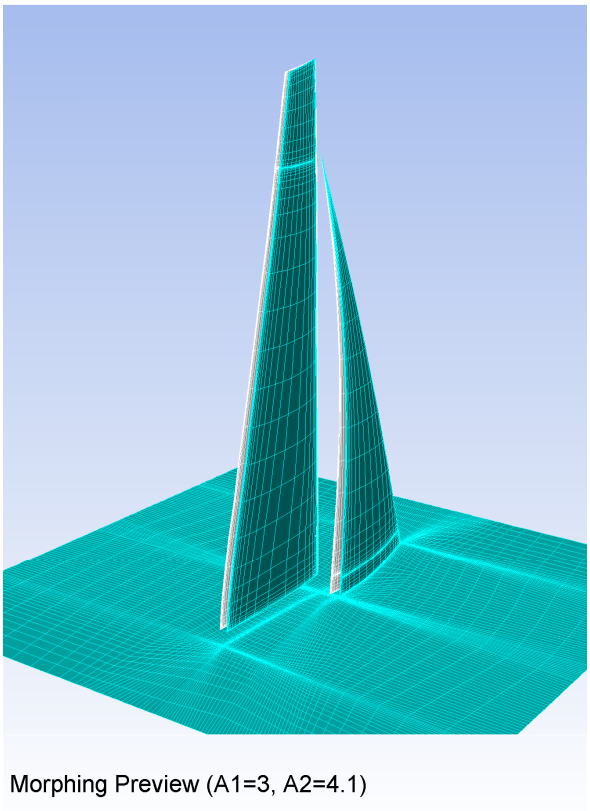

Figure 7: Morphing preview at G4M4.

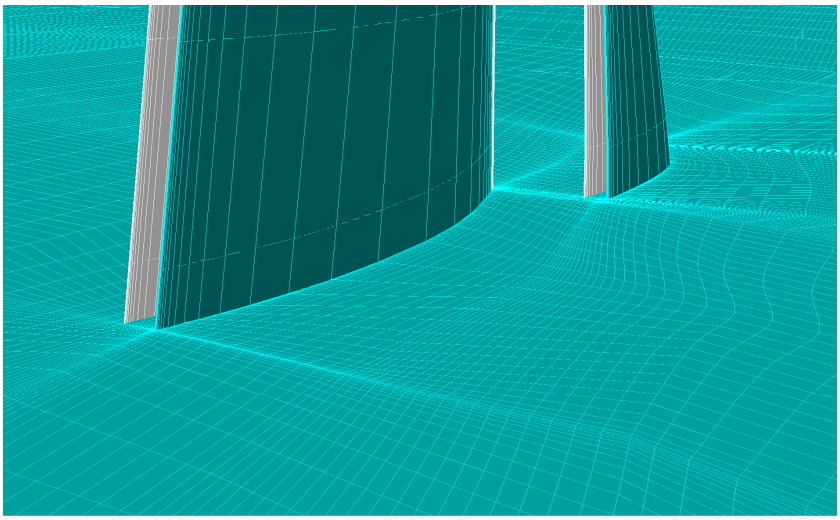

Figure 8: Morphing preview at G4M4 on a horizontal plane at one-metre height.

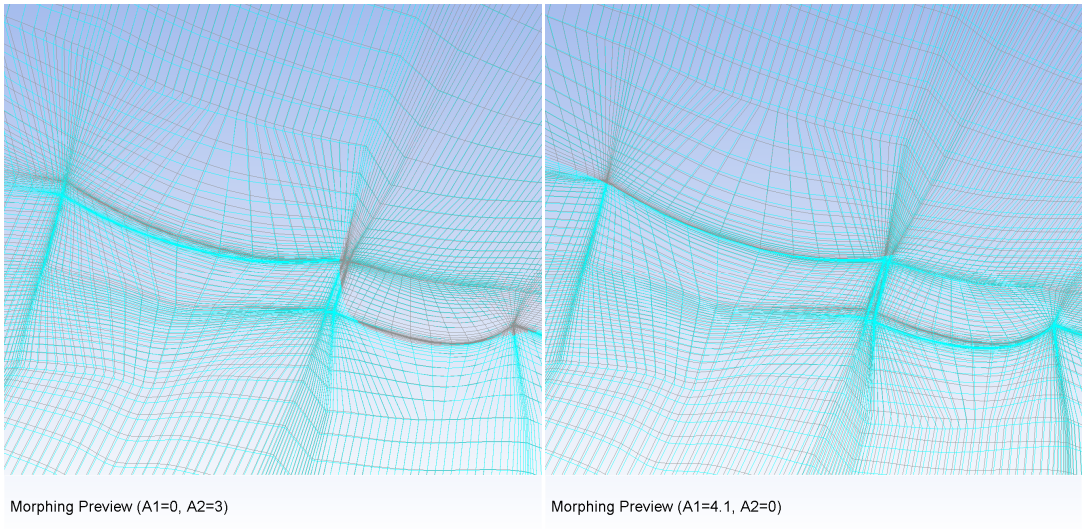

Figure 9: Orthographic view of internal morphed mesh at G1M4 and G4M1 superimposed with original mesh.

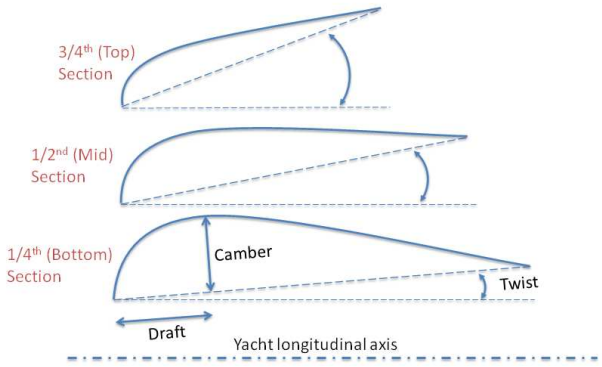

Figure 10: Definition of twist draft and camber parameters.

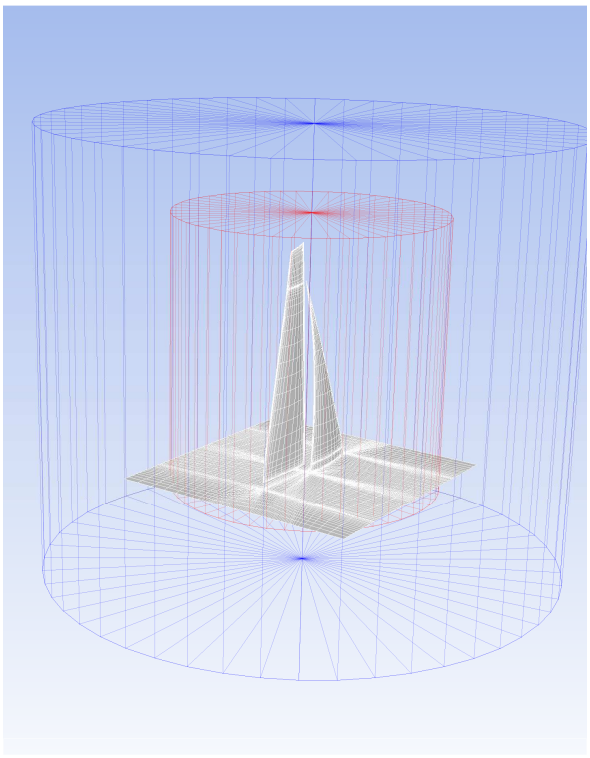

Figure 11: Encapsulation cylinders used to control AWA.

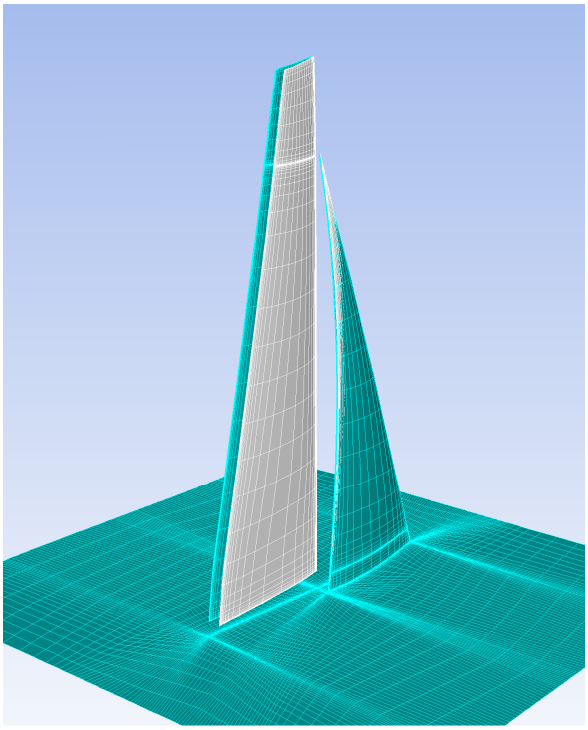

Figure 12: Morphing preview at AWA=-5°.

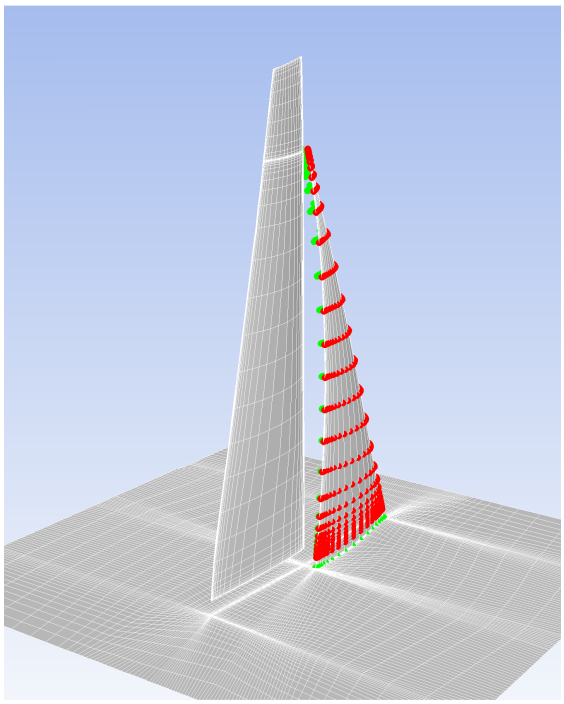

Figure 13: First step of setup for heeling angle. Local control of Genoa Sail used to deal with deformable buffer.

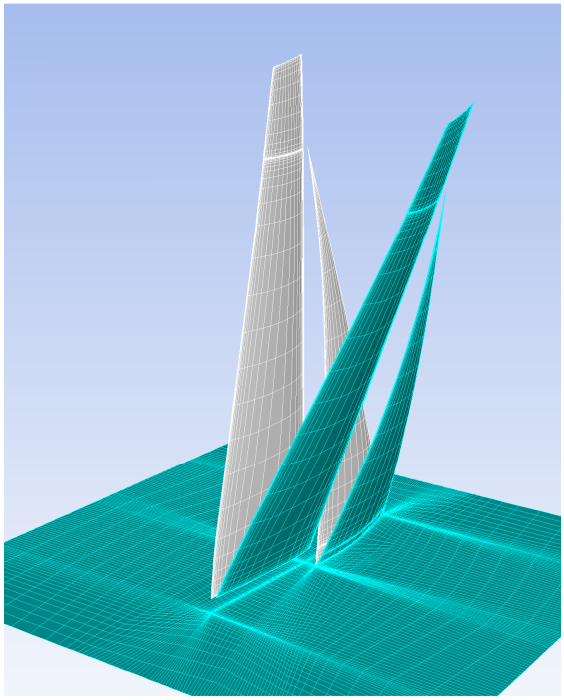

Figure 14: Morphing preview at Heeling Angle =20°.

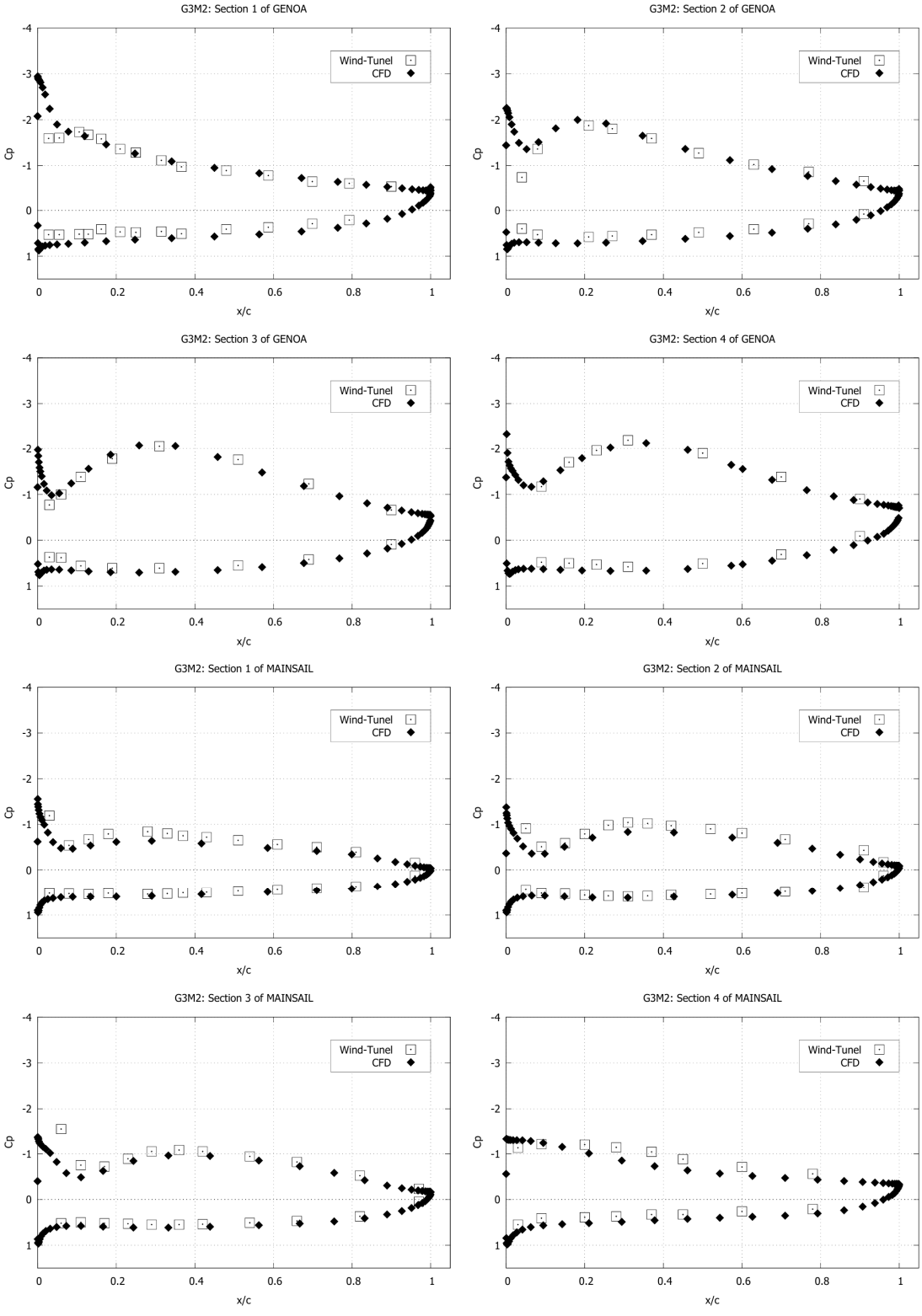

Figure 15: Measured and computed C_p on the four sail sections of the genoa (left) and mainsail (right).

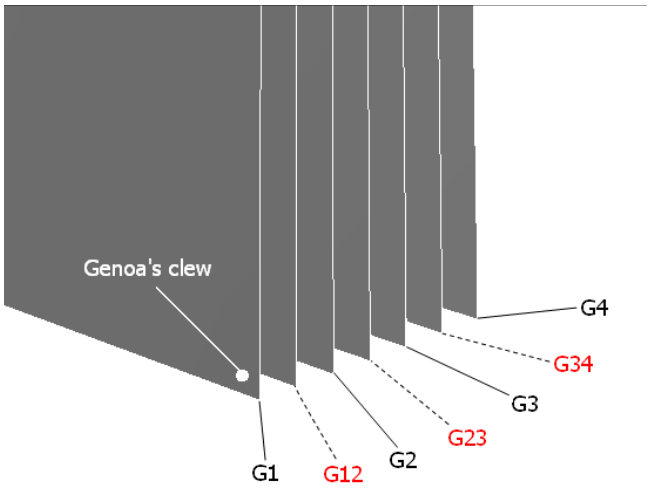

Figure 16: Intermediate positions (dotted lines) of the genoa explored with the morphing technique.

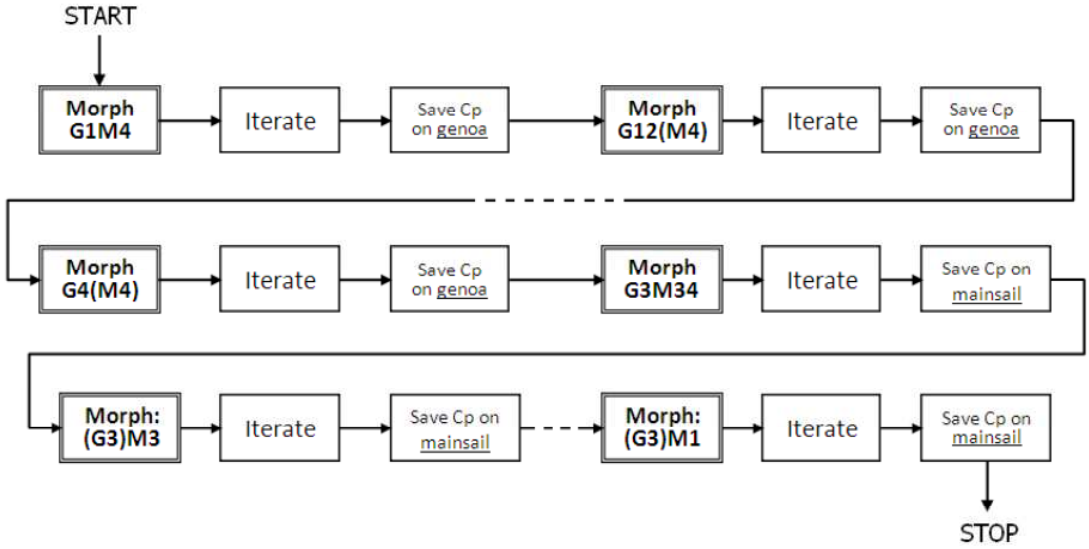

Figure 17: Description of the simulation performed using the morphing technique

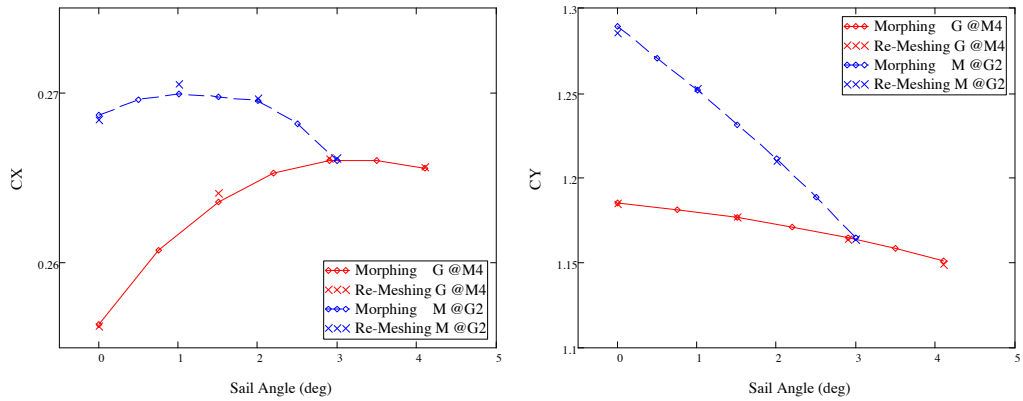

Figure 18: CX (left) and CY (right) values obtained for Genoa Sail Angle sweep at constant Main value M4 and Main angle sweep at constant Genoa value G2.

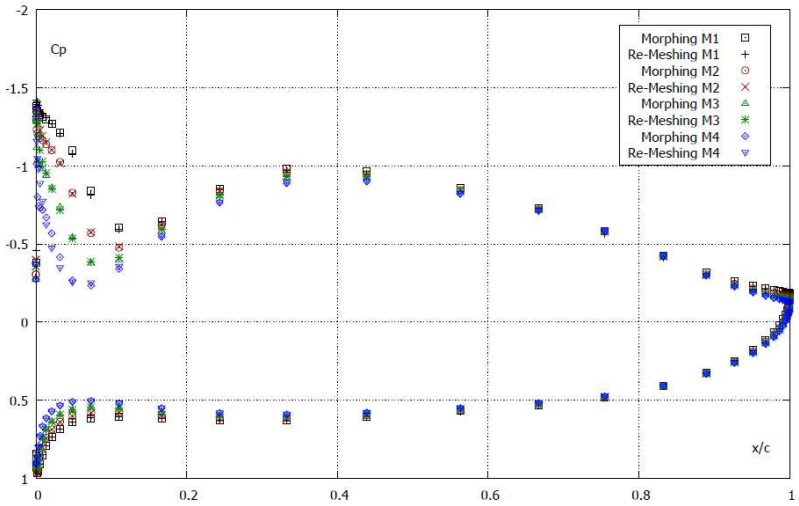

Figure 19: Overlapping of the C_p computed from both re-meshing and morphing at section 3 of the mainsail.

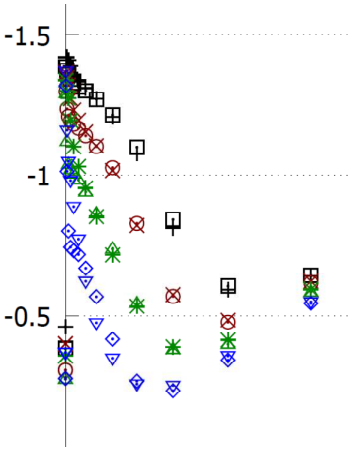

Figure 20: Zoom at the suction-peak region of the leeward side in Figure 19.

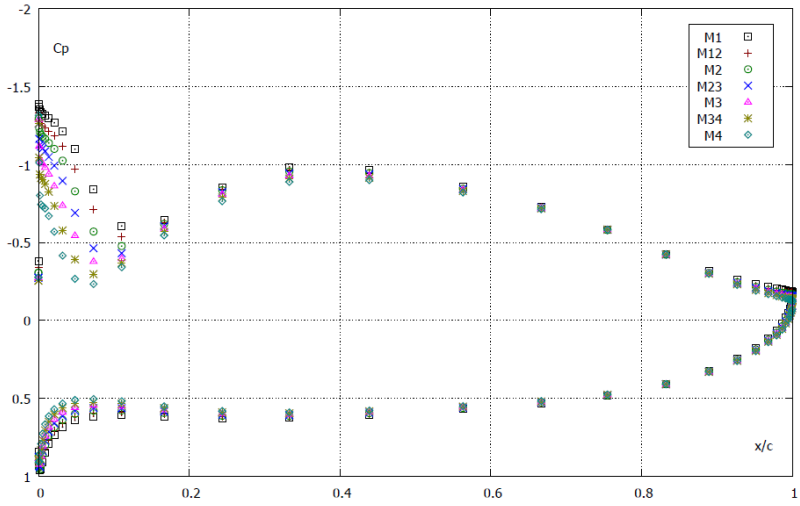

Figure 21: Intermediate C_p evolution computed using morphing.

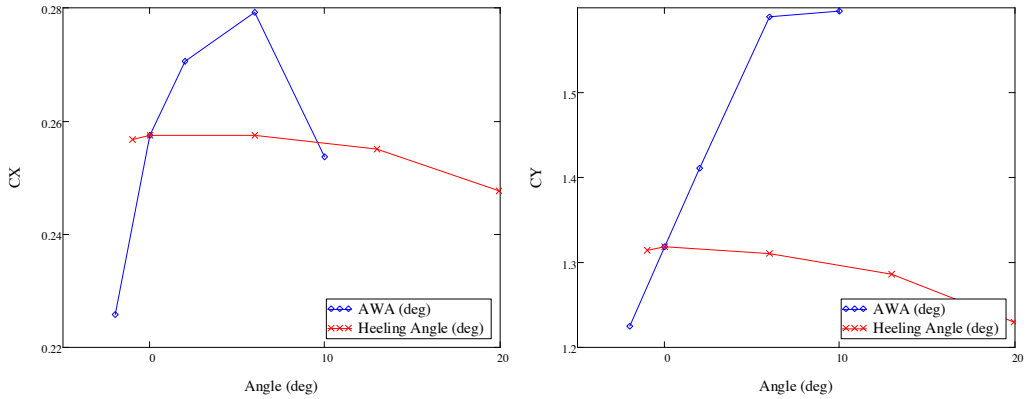

Figure 22: CX (left) and CY (right) for different AWA variations ($AWA - 19\ °$) and heel angles

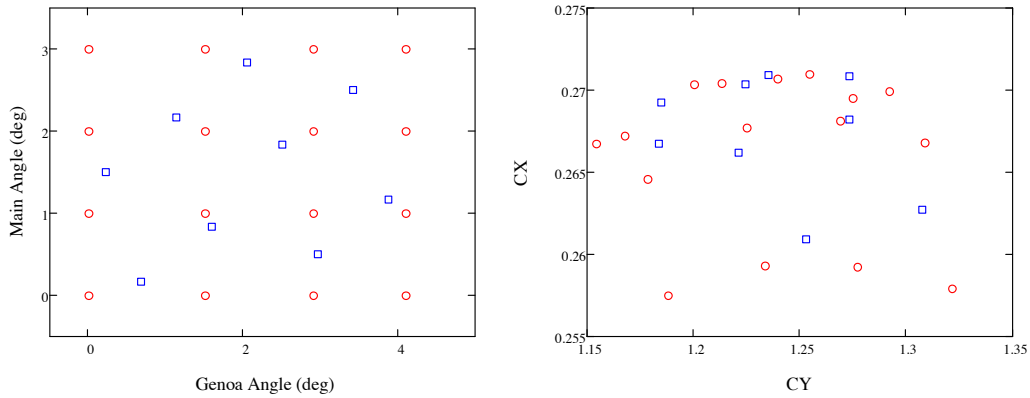

Figure 23: Design points arrangement (left) for the 16 points full factorial distribution (circles) and the 9 points optimal space filling distribution (squares), and corresponding output value as CX and CY pairs (right).

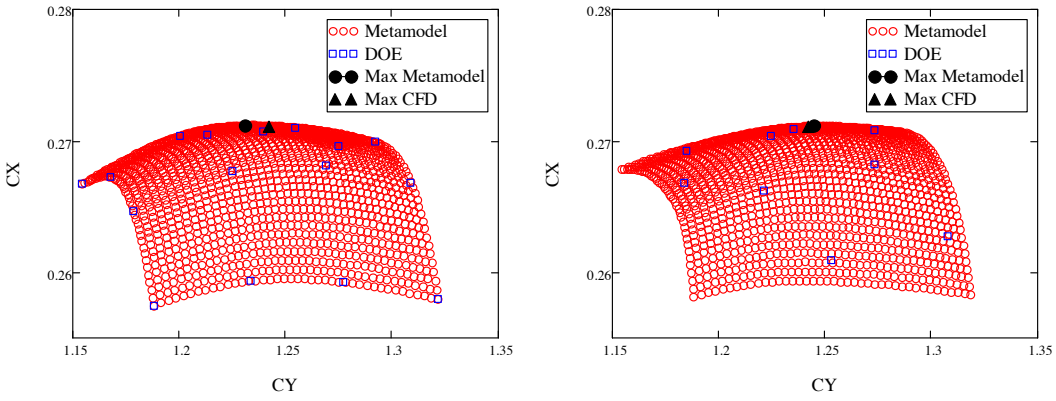

Figure 24: CX and CY results using metamodel for the 16 points full factorial distribution and the 9 points optimal space filling distribution.

Table 1: Typical Radial Basis functions.

Radial Basis Functions (RBF)	$\varphi(r)$

with global support	
Spline type (R_n)	$r^n, n\ odd$
Thin plate spline (TPS_n)	$r^n \log(r), n\ even$
Multiquadric(MQ)	$\sqrt{1+r^2}$
Inverse multiquadric (IMQ)	$\frac{1}{\sqrt{1+r^2}}$
Inverse quadratic (IQ)	$\frac{1}{1+r^2}$
Gaussian (GS)	e^{-r^2}
Radial Basis Functions (RBF) with compact support	$\varphi(r) = f(\xi), \xi \leq 1, \xi = \frac{r}{R_{sup}}$
Wendland C^0 (C0)	$(1-\xi)^2$
Wendland C^2 (C2)	$(1-\xi)^4(4\xi+1)$
Wendland C^4 (C4)	$(1-\xi)^6\left(\frac{35}{3}\xi^2+6\xi+1\right)$

Table 2: Morphed meshes quality vs. shape parameter at limit levels.

Configuration	Foresail Sheeting Angle (G)	Mainsail Sheeting Angle (M)	Minimum Ortho Quality	Maximum Aspect Ratio
G1M1	0°	0°	1.64e-02	1.555e+03
G4M1	4.1°	0°	1.38e-02	1.539e+03
G1M4	0°	3.0°	1.63e-02	1.549e+03
G4M4	4.1°	3.0°	1.41e-02	1.539e+03

Table 3: V&V of the L_2 norm of C_p on the four sail sections of the genoa and the mainsail.

	Genoa				Mainsail			
	Sec. 1	Sec. 2	Sec. 3	Sec. 4	Sec. 1	Sec. 2	Sec. 3	Sec. 4
U_g	0.064	0.018	0.007	0.021	0.028	0.064	0.150	0.068
U_c	0.021	0.021	0.021	0.021	0.021	0.021	0.021	0.021
U_{num}	0.085	0.039	0.028	0.042	0.049	0.085	0.171	0.089
U_{exp}	0.681	0.703	0.687	0.660	0.811	0.811	0.764	0.687
U_{val}	0.687	0.704	0.688	0.661	0.812	0.815	0.783	0.693
$\left\lvert \lVert C_p \rVert_{L2}^{num} - \lVert C_p \rVert_{L2}^{exp} \right\rvert$	0.571	0.384	0.169	0.035	0.144	0.227	0.168	0.023
Validation	yes	yes	yes	Yes	yes	yes	yes	yes

Table 4: Comparison between CX and CY at same configuration computed using re-meshing vs mesh morphing.

Configuration	Foresail Sheeting Angle (G)	Mainsail Sheeting Angle (M)	dCX(%)	dCY(%)
G1M4	0.0°	3.0°	0.047	0.05
G2M4	1.4°	3.0°	-0.195	-0.033
G3M4	2.7°	3.0°	-0.054	0.107
G4M4	4.1°	3.0°	-0.026	0.186
G2M1	2.7°	0.0°	0.107	0.314
G2M2	2.7°	1.0°	-0.21	-0.041
G2M3	2.7°	2.0°	-0.041	0.131
G2M4	2.7°	3.0°	-0.039	0.102

Table 5: 16 points Full Factorial DOE table.

Case	G	M	CX	CY
1	0,0	0,0	0,258	1,322
2	0,0	1,0	0,259	1,277
3	0,0	2,0	0,259	1,234
4	0,0	3,0	0,257	1,188
5	1,5	0,0	0,267	1,309
6	1,5	1,0	0,268	1,269
7	1,5	2,0	0,268	1,225
8	1,5	3,0	0,265	1,179
9	2,9	0,0	0,270	1,292
10	2,9	1,0	0,271	1,255
11	2,9	2,0	0,270	1,213
12	2,9	3,0	0,267	1,168
13	4,1	0,0	0,270	1,275
14	4,1	1,0	0,271	1,239
15	4,1	2,0	0,270	1,200
16	4,1	3,0	0,267	1,154

Table 6: 9 points Optimal Space Filling DOE table.

Case	G	M	CX	CY
1	3,0	0,5	0,271	1,273
2	3,9	1,2	0,271	1,235
3	1,1	2,2	0,266	1,221
4	2,5	1,8	0,270	1,225
5	0,7	0,2	0,263	1,308
6	1,6	0,8	0,268	1,273
7	2,1	2,8	0,267	1,184
8	3,4	2,5	0,269	1,185
9	0,2	1,5	0,261	1,253